J Mater Sci (2021) 56:17568–17583

Chemical routes to materials

Synthesis and characterisation of $M_xFe_{3-x}O_4$ (M = Fe, Mn, Zn) spinel nanoferrites through a solvothermal route

Hossein Etemadi[1] and Paul G. Plieger[1,*]

[1] School of Fundamental Sciences, Massey University, Private Bag 11 222, Palmerston North, New Zealand

Received: 1 July 2021
Accepted: 14 August 2021
Published online: 30 August 2021

ABSTRACT

Given the technical hurdles associated with the thermal decomposition method for the synthesis of monodisperse nanocrystals, metal spinel nanoferrites $M_xFe_{3-x}O_4$ (M = Fe, Mn, Zn) were prepared by the solvothermal method. Structural, morphological and magnetic characterisations were completed using powder X-ray diffraction (XRD), transmission electron microscopy (TEM), thermogravimetric analysis (TGA), energy-dispersive spectroscopy (EDS), atomic absorption spectroscopy (AAS), vibrating sample magnetometry (VSM) and X-ray photoelectron spectroscopy (XPS) techniques. The size of the synthesised nanoferrites spanned from 7 to 16 nm based on TEM results. EDS, AAS and XPS evidenced successful doping of Zn^{2+} and Mn^{2+} into the Fe_3O_4 structure. XRD revealed the expansion of the cell unit of Fe_3O_4 with the substitution of the larger Zn^{2+} and Mn^{2+} ions. All prepared nanoferrites presented with superparamagnetism at room temperature (300 K) with a blocking temperature less than room temperature ($T_B < T$).

Handling Editor: Dale Huber.

Address correspondence to E-mail: p.g.plieger@massey.ac.nz

https://doi.org/10.1007/s10853-021-06450-8

GRAPHICAL ABSTRACT

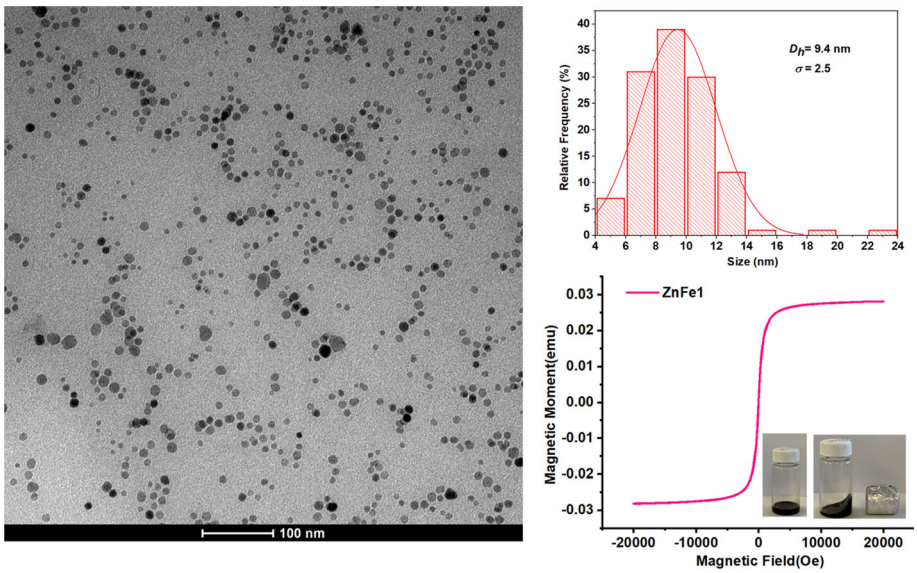

Introduction

The synthesis of small (diameter < 30 nm) iron oxide (Fe_3O_4 or γ-Fe_2O_3) nanoparticles (NPs) with narrow size distributions (< 5%) and pronounced saturation magnetisation (M_s) is an important prerequisite for their potential technological applications [1, 2]. Magnetite (Fe_3O_4) crystallises in a cubic inverse spinel configuration where Fe^{3+} ions are evenly distributed among the tetrahedral (A) and octahedral (B) sites and Fe^{2+} ions occupy the remaining octahedral sites, yielding the empirical formula $[Fe^{3+}]_A[Fe^{3+}Fe^{2+}]_BO_4$ [3, 4]. Typically, Fe_3O_4 NPs exhibit lower saturation magnetisation values (50–60 emu/g) than bulk Fe_3O_4 (85–100 emu/g) at 300 K, induced by a large spin disorder on their surface [5]. In recent years, several strategies have been considered to improve their M_s by tuning their geometry, size, size distribution and composition. One potential strategy to enhance the M_s value of magnetite is to substitute Fe^{2+} with M^{2+} cations (M = Mn, Co, Ni) [3, 6, 7]. This has been achieved through several synthetic protocols such as sol–gel pyrolysis [8], reverse micelle emulsion [9], polyol [10], solvothermal [11], and co-precipitation [12] techniques. Nevertheless, technological success in the synthesis of single-domain crystalline nanoferrites of low dispersity has been limited.

The thermal decomposition method has been proposed for the synthesis of monodisperse nanoferrites with high crystallinity. This method involves the decomposition of metal precursors, such as metal carbonyls $M(CO)_5$ [13], metal acetylacetonates $M(acac)_3$ [14] and iron oleate [2], in high-boiling point organic solvents at very high temperatures (∼ 320 °C) and in the presence of surfactants. It encourages the synthesis of monodisperse Fe_3O_4 and analogous $M_xFe_{3-x}O_4$ nanocrystals of great size uniformity, crystallinity and well-shaped configurations. Consequently, various nanoferrites such as Fe_3O_4 [15, 16], $Li_{0.3}Zn_{0.3}Co_{0.1}Fe_{2.3}O_4$ [17], $Zn_xFe_{3-x}O_4$ [18], $Mg_xMn_{1-x}Fe_2O_4$ [19], $Mn_{0.5}Zn_{0.5}Fe_2O_4$[20], $MgFe_2O_4$ [21], $Co_{0.03}Mn_{0.28}Fe_{2.7}O_4$ [22], $Mn_xZn_{1-x}Fe_2O_4$ [23] and $Co_xFe_{3-x}O_4$ nanoferrites [24] have been synthesised through this method for various applications. Despite the progress in the synthesis of monodisperse crystalline nanoferrites with high precision using this method, there are still some obstacles for its practical realisation. These include the complexity of the chemical synthesis, the need for an inert (N_2) atmosphere during the reaction, the use of flammable

organic solvents at higher temperatures and the difficult separation of solvents from the product. Another disadvantage is that the synthesised nanocrystals are dispersible in organic solvents, which requires additional steps to transfer them to the aqueous phase specially for biomedical applications. To address this, exchange agents such as PEG-phospholipid (DSPE-PEG2000) [25], methoxy-polyethyleneglycol-silane—500 Da (PEG) [5], 2,3-dimercaptosuccinic acid (DMSA) [26], Acrypol 934 [27], citric acid [28] and polyvinylpyrrolidone (PVP) [29] have been utilised to help with this.

Solvothermal methods (or hydrothermal methods when water is used as the solvent) are alternative synthetic methods which encourage the synthesis of nanocrystals with definite sizes, geometries and narrow size distributions. Generally, these are conducted using an autoclave under mild conditions [30, 31]. For example, MFe_2O_4 nanoferrites (M = Co, Mn, Ni, Zn) [32], MFe_2O_4 (M = Cu, Ni) [33], MFe_2O_4 (M = Mn, Fe, Co, Ni) [34], $CoFe_2O_4$ [35], $Mg_{1-x}Zn_xFe_2O_4$ (x = 0.4–0.7) [36], $MnFe_2O_4$ and MFe_2O_4–Ag_2O (M = Zn, Co and Ni) [37] have all been synthesised using hydrothermal decomposition of metal precursors; however, the prepared nanocrystals were aggregated even in the presence of surfactants. To synthesise nanoferrites with high monodispersity, organic phase (solvothermal) decomposition of metal precursors has been examined. For example, Tian et al. synthesised ultrasmall monodispersed magnetite NPs of 4–6 nm as potential MRI contrast agents by the decomposition of $Fe(acac)_3$ in *n*-octanol. Additionally, Dendrinou-Samara et al. have utilised oleylamine (OAm) as both the solvent and surface-functionalising agent to synthesise $NiFe_2O_4$ NPs (9–11.7 nm) with M_s values of 32.0–53.5 emu/g, $CoFe_2O_4$ NPs (9–11 nm) with M_s values of 84.7–87.5 emu/g and 9-nm-sized $MnFe_2O_4$ with M_s values of 65.7 emu/g for biomedical applications. However, some aggregation was observed in the prepared nanocrystals [38–40].

In our previous work, we addressed this aggregation issue by the careful control of reaction parameters leading to highly uniform $M_xFe_{3-x}O_4$ (M = Fe, Mg, Zn) nanoferrites using a mild solvothermal route. However, we found that our particles exhibited decreased magnetisation after substituting Fe_3O_4 with diamagnetic Mg^{2+} ions [41]. Additionally, they were only dispersible in an organic solvent (hexane). In the present work, we have attempted to increase the magnetisation by the substitution of paramagnetic Mn^{2+} ions into the Fe_3O_4 structure and subsequently explored the effect of this substitution on the crystallinity and magnetisation values of bare Fe_3O_4 NPs. In addition, considering that PVP is a water-soluble stabilising agent, we replaced oleic acid (OA) with PVP in an attempt to directly synthesise water-dispersible nanoferrites without additional phase exchange treatments.

Experimental Section

Materials

Iron (III) acetylacetonate ($Fe(acac)_3 \geq 99.9\%$ trace metals basis), oleylamine (≥ 70%), polyvinylpyrrolidone (Mw ≈ 25,000), tri-n-octylphosphine oxide (TOPO, 99%), octadecene (ODC, 90%), AR grade 1,5-pentanediol, tetramethylammonium hydroxide (20% w/w) and manganese(II) chloride ($MnCl_2$) were purchased from Sigma–Aldrich. Zinc chloride ($ZnCl_2$) was purchased from Ajax Finechem. All other chemicals were of analytical grade and used as received from commercial sources without further purification.

Synthesis of $M_xFe_{3-x}O_4$ (M = Fe, Mn, Zn) spinel nanoferrites

Similar to our previous work [41], we used a solvothermal route with some modifications to develop monodisperse $M_xFe_{3-x}O_4$ (M = Fe, Mn, Zn) spinel nanoferrites. For a typical synthesis of spinel $M_xFe_{3-x}O_4$ (M = Fe, Mn, Zn) NPs, the defined amounts of metal (the Zn, Fe and Mn precursors), OAm and TOPO (Table 1) were mixed in octadecene (20 mL) under stirring (500 rpm) at 100 °C for 60 min. Polyvinylpyrrolidone (0.20 g) was dissolved in 1,5-pentanediol (5 mL) and heated to 150 °C for 60 min. The reason for using 1,5-pentanediol is to improve the solubility of PVP in octadecene.

The two solutions were then mixed and deoxygenated with Ar (2 min) and then transferred into a 100-mL polytetrafluoroethylene (PTFE)-lined autoclave. The autoclave was sealed and maintained at 200 °C for 30 min and then heated to 240 °C for 2 h. After this time, the autoclave was left to cool to RT. The $M_xFe_{3-x}O_4$ (M = Fe, Mn, Zn) nanoferrites were precipitated upon the addition of ethanol (10 mL),

Table 1 Synthesis conditions for $M_xFe_{3-x}O_4$ (M = Fe, Mn, Zn) nanoferrites

Nanoferrite	OAm (mL)	PVP (mg)	$Fe(acac)_3$ (mmol)	$ZnCl_2$ (mmol)	$MnCl_2.4H_2O$ (mmol)	TOPO (mmol)
Fe1	2.56	200	1	0	0	0.5
Fe2	3.2	200	1	0	0	0.5
MnFe1	2.56	200	0.8	0	0.2	0.5
MnFe2	3.2	200	0.8	0	0.2	0.5
ZnFe1	2.56	200	0.6	0.4	0	0.5
ZnFe2	3.2	200	0.6	0.4	0	0.5

washed with an ethanol/hexane (1:2) solution mixture several times and then dispersed in hexane for further use.

Characterisation

The structure, chemical composition and magnetic features of the synthesised nanoferrites were probed with transmission electron microscopy (TEM; Tecnai G2 Spirit Bio-TWIN), powder X-ray diffraction (XRD; Rigaku Spider X-ray diffractometer), energy-dispersive X-ray-connected scanning electron microscopy (SEM–EDX; FE-SEM FEI Quanta), atomic absorption spectroscopy (AAS; AAS-9000 spectrometer, Shimadzu), thermogravimetric analysis (TGA; TA Instruments Q500), X-ray photoelectron spectroscopy (XPS; Kratos Axis Ultra^{DLD}) and vibrating sample magnetometry (VSM; Quantum Design P935A USA, physical property measurement system (PPMS)). Further details regarding characterisation are described in the supporting information.

Results and discussion

Structural and compositional studies

In our previous research, we investigated the effect of various experimental conditions and reaction parameters to successfully synthesise monodisperse $M_xFe_{3-x}O_4$ (M = Fe, Mg, Zn) spinel nanoferrites [41]. The optimal conditions for the synthesis of a range of monodisperse NPs with high uniformity were found to be a 1:4 OA to OAm molar ratio, 0.5 mmol TOPO, 120-min reaction time and a temperature of 240 °C [41]. The resulting nanoparticles were not dispersible in water. Therefore, phase exchange treatment was performed using tetramethylammonium hydroxide to transfer hexane-dispersible nanoferrites to the aqueous phase.

In an attempt to directly synthesise water-dispersible nanoferrites without an additional ligand exchange process, we replaced OA with PVP. The rational is that polyvinylpyrrolidone (PVP) is a non-charged amphiphilic polymer which can be dissolved in either water or organic solvents [42]. Huang et al. synthesised water-dispersible stable colloidal Fe_3O_4 nanocrystals through thermal decomposition of $Fe(Co)_5$ in the presence of PVP as the sole stabiliser for MRI applications [25]. It was expected that PVP molecules adsorbed on the particle surface would help to improve the dispersibility of the resultant nanocrystals in water. However, the obtained nanoferrites were not water dispersible due to the presence of OAm and TOPO in the reaction medium.

The TEM images of Fe1 and Fe2 (Fig. 1a, b) show the arrangement of NPs in a close-packed assembly. The Fe1 and Fe2 NPs exhibit predominantly spherical shapes with mean particle sizes of 7.9 ± 1.2 nm and 8.5 ± 2.2 nm, respectively (Fig. 1c, d). Substitution of Mn^{2+} ions into Fe_3O_4 results in deformed NPs with larger sizes than that of Fe1–2 as shown in the corresponding TEM micrographs of MnFe1 (Fig. 2a) and MnFe2 (Fig. 2b). The average particle sizes were determined to be 8.9 ± 1.9 nm (Fig. 2c) and 10.6 ± 2.9 nm (Fig. 2d) for MnFe1 and MnFe2, respectively. The TEM images of ZnFe1 (Fig. 3a) and ZnFe2 (Fig. 3b) show some well-separated spherical particles of good size uniformity. The ZnFe1 and ZnFe2 NPs have average particle sizes of 9.4 ± 2.5 nm (Fig. 3c) and 10.3 ± 2.1 nm (Fig. 3d), respectively. Increasing the concentration of OAm has resulted in both increased [43] and decreased size effects in the past [41]. In terms of size and morphology, an increase in the OAm amount in the

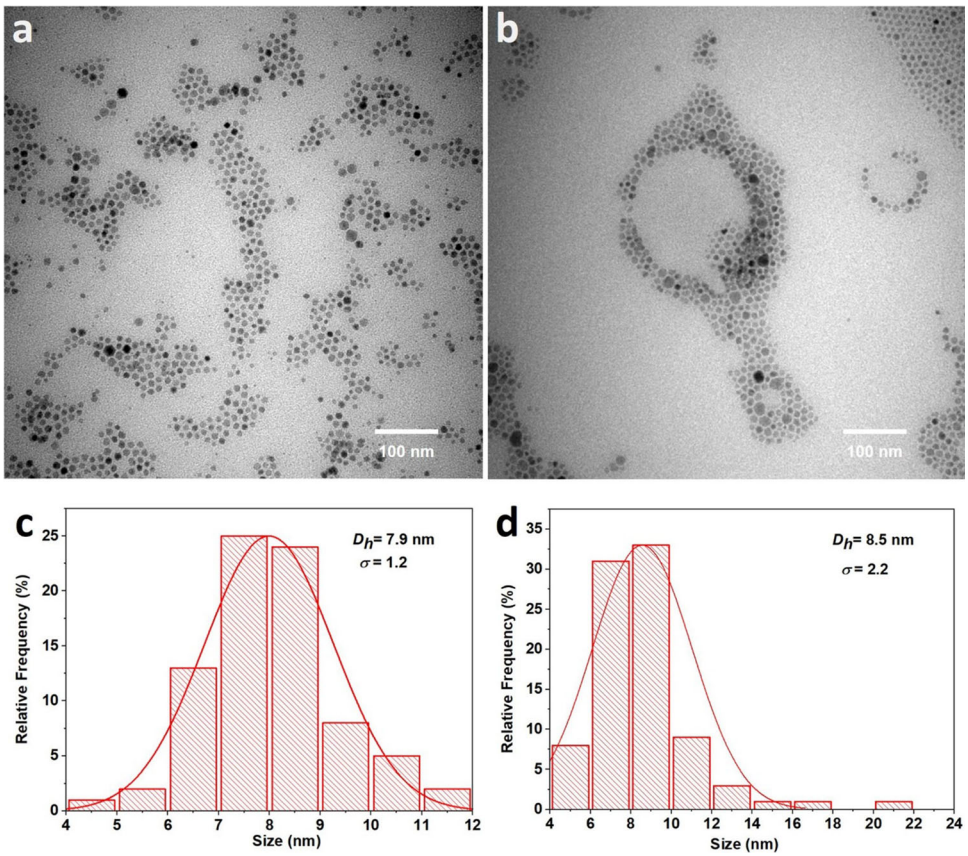

Figure 1 TEM images of the synthesised Fe1 (**a**) and Fe2 (**b**) NPs at different magnifications. Insets: Size distribution of Fe1 (**c**) and Fe2 (**d**) with mean size (D_h) and standard deviation (σ).

present study does not appear to have had an influence (within experimental error).

The crystalline phase and purity of $M_xFe_{3-x}O_4$ (M = Fe, Mg, Zn) nanoferrites were studied by powder X-ray diffraction (PXRD) (Figs. 4 and S1). The XRD patterns of Fe_3O_4 NPs (Fe1 and Fe2) at 2θ = 18.50°, 30.1°, 35.6°, 43.1°, 53.2°, 57.2° and 63° can be indexed to the crystallographic planes of (111), (220), (311), (400), (422), (511) and (440) [44, 45]. Importantly, no other impurities corresponding to other iron oxide crystal phases such as γ-Fe_2O_3 (additional peaks at 2θ = 23.77° (210) and 26.10° (211) (JCPDS no. 39-1346)) [46, 47], α-Fe_2O_3 (2θ = 24.1° (012), 33.1° (104), 40.8° (113), 49.4° (024), 53.9° (116), 57.4° (018), 62.3° (214) and 63.9° (300) (JCPDS no. 24-0072)) [48] or FeO (2θ = 36.0° (113), 41.8° (200) and 60.7° (220) (JCPDS no. 06-0615))[49] were detected in the XRD patterns, confirming the purity of the synthesised Fe_3O_4 crystals.

The average crystallite sizes of Fe1 and Fe2 calculated from the Debye–Scherrer equation were 7.2 ± 0.89 nm and 6.9 ± 0.38 nm, respectively. Considering the strong Bragg reflection peak (Miller index 3 1 1), the lattice spacing (d) and lattice constant (a) were determined for all $M_xFe_{3-x}O_4$ (M = Fe, Mn, Zn) nanoferrites (Table 2). The lattice constants were both 8.3481 Å for Fe1 and Fe2 NPs, consistent with a = 8.35 Å reported for Fe_3O_4 NPs [50].

The XRD patterns of Mn-doped Fe_3O_4 are well matched with the single-phase spinel cell geometry. The Bragg diffraction peaks at 2θ values of 18.5°, 30.1°, 35.5°, 42.80°, 52.8°, 57.1° and 62.5° corresponded to the crystal reflection planes of (111), (220), (311), (400), (422), (511) and (440) (JCPDS no. 74-2403) [51]. There is no evidence of impurities related to manganese oxide secondary phases such as α-MnO_2 (2θ = 12.7° (110), 18.1° (200), 28.8° (310), 37.5° (211), 42.1° (301), 49.9° (411), 56.2° (600) and 60.3° (521) (JCPDS no. 44-0141)) [52] or MnO_2 (2θ = 37.12° (100) and 66.75° (110) (JCPDS no. 30-0820)) [53]. This confirms that Mn^{2+} ions substituted Fe^{2+}/Fe^{3+} in the Fe_3O_4 crystal unit rather than being distributed on the surface of Fe_3O_4 as a manganese oxide. The (311) crystal plane of Mn-doped Fe_3O_4 shifted from 2θ = 35.6° for Fe1 to 35.56° for MnFe1. Moreover, a increased from 8.3481 Å to 8.3800 Å and d increased from 2.5170 Å to 2.5266 Å [53]. The diffraction peaks of $ZnFe_2O_4$ representing the (111), (220), (311), (400),

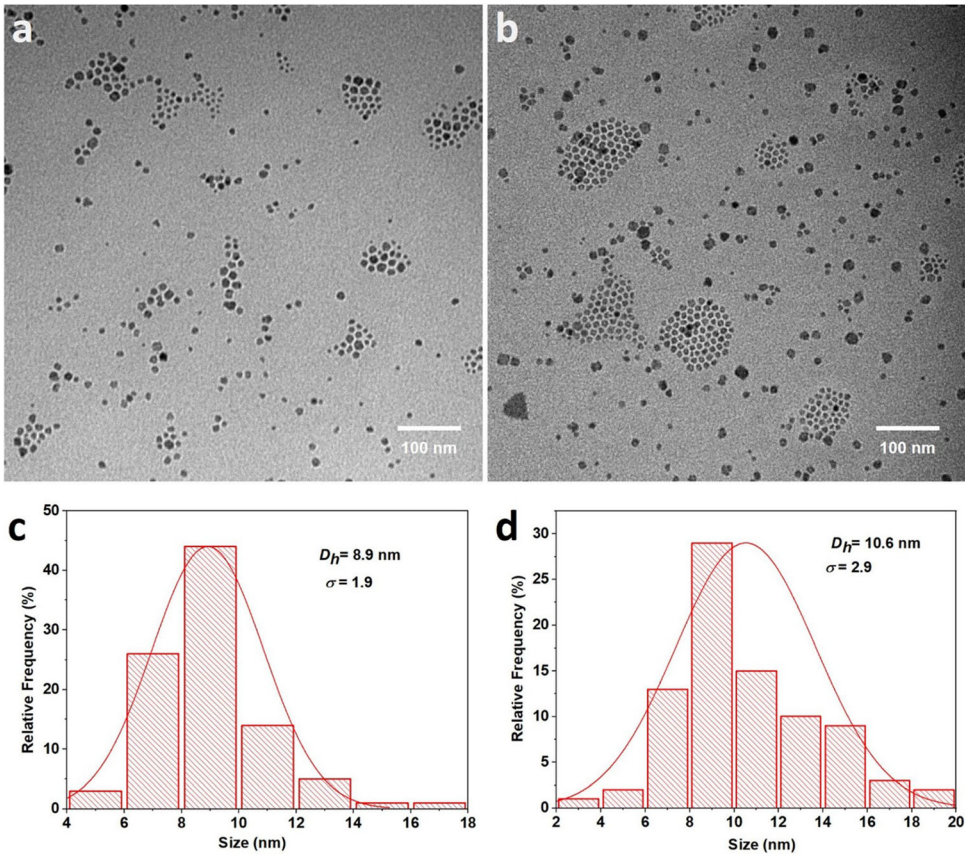

Figure 2 TEM images of the synthesised MnFe1 (**a**) and MnFe2 (**b**) NPs at different magnifications Insets: Size distribution of MnFe1 (**c**) and MnFe2 (**d**) with mean size (D_h) and standard deviation (σ).

(422), (511) and (440) crystal planes agree well with the standard cubic spinel $ZnFe_2O_4$ [54].

Importantly, sharper peaks were observed in the XRD patterns of Zn-doped Fe_3O_4, which suggested greater crystallinity compared to undoped Fe_3O_4. No secondary phases of zinc oxides (2θ = 31.7° (100), 34.4° (002), 36.2° (101), 47.5° (105) and 56.5° (110)) (JCPDS no. 36-1451) were detected, indicating the purity of the crystals [55, 56]. Nevertheless, in line with Mn-doped Fe_3O_4, the (311) crystal plane of Zn-doped Fe_3O_4 slightly shifted from 2θ = 35.64° for Fe1 to 35.52° for ZnFe1 (Fig. 4b, labelled with a #). Furthermore, the corresponding lattice constant and lattice spacing increased from 8.3481 to 8.3754 Å and 2.5170 to 2.5253 Å. The increase in lattice parameters (expansion of the unit cell volume) of Fe_3O_4 after doping is due to the replacement of Fe^{3+} (r_{ionic} = 0.64 Å) [57] and/or Fe^{2+} ions (r_{ionic} = 0.76 Å) [58] with larger Mn^{2+} (r_{ionic} = 0.80 Å) [58] or Zn^{2+} ions (r_{ionic} = 0.74 Å) [59]. Lattice expansion of Fe_3O_4 by Zn^{2+} [58, 60] or Mn^{2+} [61] has been previously reported.

The physical sizes obtained from TEM are larger for the ZnFe nanoferrites than that of the crystallite sizes measured by XRD, with the remaining nanoferrites all within experimental error. This increase in size for the ZnFe nanoferrites could be ascribed to the fact that the reaction performance does not always lead to single crystal particles.

Thermogravimetric analysis (TGA) under an N_2 flow with a heating rate of 10 °C/min from room temperature to 800 °C was used to quantitatively determine the organic fraction of nanoferrites (Fig. 5). The fraction of inorganic cores inside the nanoferrites is represented by the mass percentage of the residue; hence, the weight fraction of the surfactants in the nanoferrites can be established.

The first loss of mass below 200 °C in all samples refers to the removal of water or organic solvents from the nanoferrite surface [62]. The mass loss between 250 and 350 °C in the thermograms of all samples can be attributed to the decomposition of the free surfactants adsorbed on the surface of the NPs [63, 64]. The mass loss between 450 and 620 °C corresponds to the decomposition of directly attached surfactants [65]. The final loss of weight between 600 and 750 °C for all nanoferrites can be assigned to the reduction of the inorganic metal core under a N_2

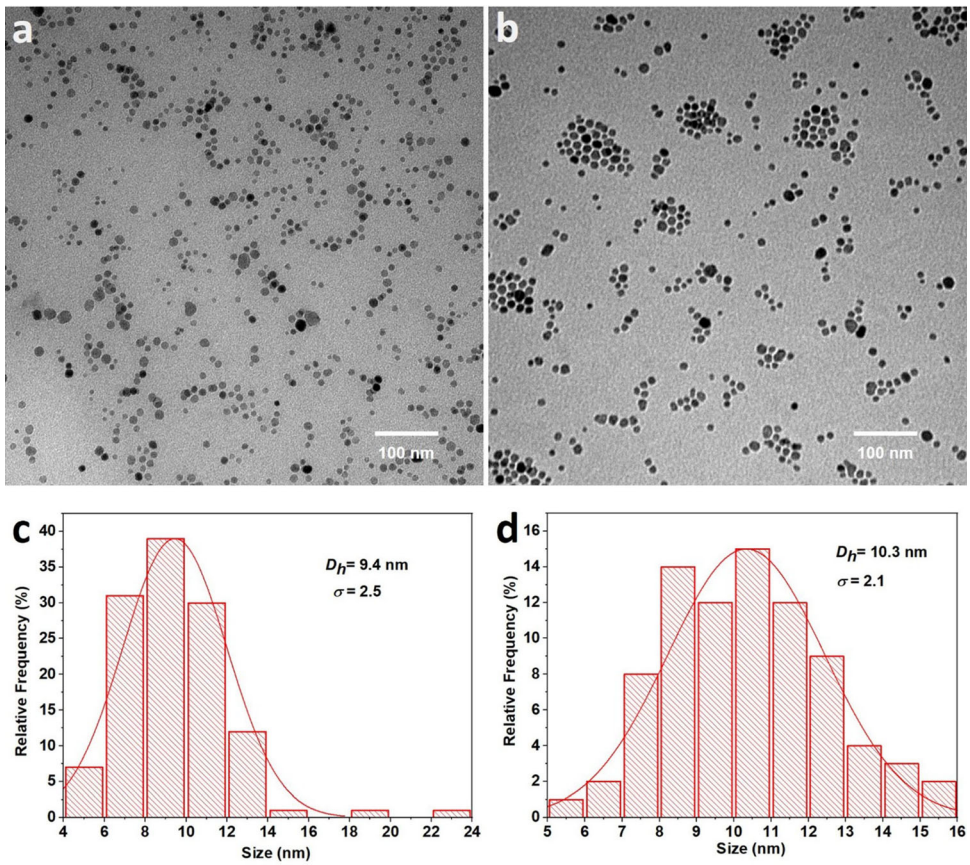

Figure 3 TEM images of the synthesised ZnFe1 (**a**) and ZnFe2 (**b**) NPs at different magnifications. Insets: Size distribution of ZnFe1 (**c**) and ZnFe2 (**d**) with mean size (D_h) and standard deviation (σ).

atmosphere. For Fe1, the loss of weight was a two-stage process between 600 and 700 °C and 700 and 750 °C. Ayyappan et al. and Mameli et al. have reported the same behaviour for $CoFe_2O_4$ [66] and $Zn_xCo_{1-x}Fe_2O_4$ ($0 < x < 0.6$) nanoferrites [18].

Notably, there are discontinuities in the thermograms of MnFe2 (just above 400 °C and at approximately 500 °C), Fe1 (just past 600 °C) and MnFe1 (at approximately 300 and 500 °C). This may be the result of the instrument being slightly bumped during the measurements.

The fraction of stabilising surfactants around the nanoferrites tends to reduce with increased magnetic core size (Table 2). Larger nanocores possess lower surface-to-volume ratios, which results in less active sites available for binding surfactants [67, 68].

EDS spectra of nanoferrites were obtained through line scans of selected sites at various magnifications to analyse the chemical compositions in a semi-quantitative manner. The EDS results for all nanoferrites collected from different positions exhibited similar atomic percentages (At%), indicating the composition homogeneity of the nanoferrites [69]. For instance, the At% of Mn atoms were 4.81% and 4.03% for MnFe1 and MnFe2 NPs, respectively. A similar trend could also be seen in EDS results of Fe1–2 and Zn1–2 as depicted in Figures S2–S4.

Peaks corresponding to C atoms, due to surfactants and the carbon coating prior to analysis, were observed in the EDS spectra of all nanoferrites. The characteristic peaks for Fe and O were observed in the EDS spectra of Fe1–2 (Figure S2). The EDS spectra of MnFe1–2 contained Fe, Mn and O peaks (Figure S3), and the EDS spectra of ZnFe1–2 featured Fe, Zn and O peaks (Figure S4). Notably, in the case of Mn-doped Fe_3O_4 NPs, the signals of Mn and Fe overlap at 6.5 keV. This has also been observed for other Fe–Mn nanoferrites [53, 70] and is due to the close energy levels of Mn K_β and Fe K_α, which makes it difficult to distinguish them on EDS spectra. Based on EDS analysis, the Fe/O, Mn/Fe/O and Zn/Fe/O atomic ratios differed from the expected stoichiometries.

Atomic absorption spectroscopy (AAS) was used to determine the experimental chemical formula of $M_xFe_{3-x}O_4$ nanoferrites (Table 3). The calibration

curve equations and R^2 for each analyte along with the experimental absorption values are presented in Figures S5–S7 for the nanoferrites. Consistent with the EDS results, the molar ratios and chemical formula derived from AAS results were not in agreement with the corresponding theoretical values. Our group, Hu et al. and Oberdick et al. have also reported this deviation from theoretical stoichiometry in $M_xFe_{3-x}O_4$ $Co_xFe_{3-x}O_4$ and core/shell $Fe_3O_4/Mn_xFe_{3-x}O_4$ NPs [71, 72]. This might be due to the different decomposition temperatures of Fe $(acac)_3$, $MnCl_2$ and $ZnCl_2$ salts [73]. In addition, the large magnitude of surfactants used in the synthetic process may alter the decomposition temperatures of $Fe(acac)_3$, $MnCl_2$ and $ZnCl_2$ salts and influence the growth mechanism [71, 74].

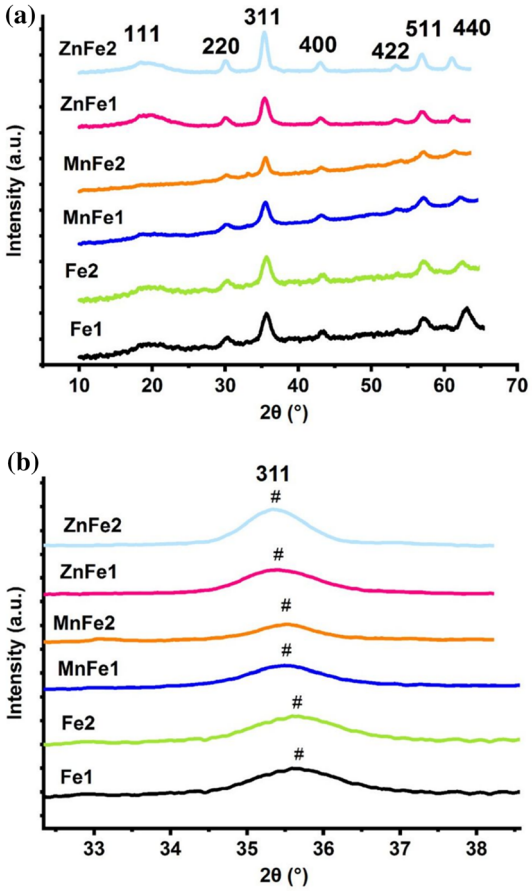

Figure 4 **a** Powder X-ray diffraction patterns and **b** the highlighted (311) diffraction peaks of $M_xFe_{3-x}O_4$ (M = Fe, Mg, Zn) nanoferrites.

The chemical compositions and oxidation states of $M_xFe_{3-x}O_4$ (M = Fe, Mn, Zn) nanoferrites were investigated via X-ray photoelectron spectroscopy (XPS). The C 1*s* signal at 284.6 eV (adventitious carbon) was utilised as an energy reference in order to calibrate the binding energy (B.E) scale ranging from 0 to 1300 eV. Wide-scan surveys confirmed the peaks of carbon (C 1*s*), oxygen (O 1*s*), iron (Fe 2*p*), zinc (Zn 2*p*) and manganese (Mn 2*p*) photoelectron lines recorded at B.E values of 280–300 eV, 520–550 eV, 702–750 eV, 630–665 eV and 1015–1055 eV, respectively (Figs. 6 and S8–S12). A sharp peak at 285 eV was observed in the high-resolution C 1*s* XPS spectra of all nanoferrites, which corresponded to the C–C bond of surfactants and adventitious carbon [75, 76]. For all nanoferrites, the O 1*s* core-level spectrum showed a low-intensity signal centred at lower B.E value of ~ 530 eV, attributed to the metal–oxygen bonds of $M_xFe_{3-x}O_4$ [77, 78], and a larger peak at ~ 532 eV assigned to carboxylate groups [76].

For the Fe1 NPs, the Fe 2*p* core-level spectrum indicates the absence of Fe ions on the surface (Fig. 6). For the Fe2 NPs, the doublet peaks centred at B.E values of 710.6 and 723.8 eV are ascribed to Fe $2p_{3/2}$ and Fe $2p_{1/2}$ of Fe^{3+} in Fe_3O_4 (Figure S8) [79]. The spin–orbit splitting energy difference was 13.2 eV

Table 2 Calculated values of size and lattice parameters for $M_xFe_{3-x}O_4$ (M = Fe, Mn, Zn) nanoferrites

Nanoferrites	Crystallite size (nm) XRD	Size (nm) TEM	Position of 311 peak in degree (θ)	*d*, Lattice spacing (Å)	*a*, Lattice constant (Å)	Organic content (%)
Fe1	7.2 ± 0.89	7.9 ± 1.2	35.64	2.5170	8.3481	72.3
Fe2	6.7 ± 0.38	8.5 ± 2.2	35.64	2.5170	8.3481	74.84
MnFe1	8.8 ± 1.4	8.9 ± 1.9	35.5	2.5266	8.3800	66.41
MnFe2	9.4 ± 0.89	10.6 ± 2.9	35.54	2.5239	8.3709	56.03
ZnFe1	5.3 ± 1.46	9.4 ± 2.5	35.4	2.5336	8.4029	81.70
ZnFe2	5.7 ± 1.35	10.3 ± 2.1	35.5	2.5266	8.3800	76.11

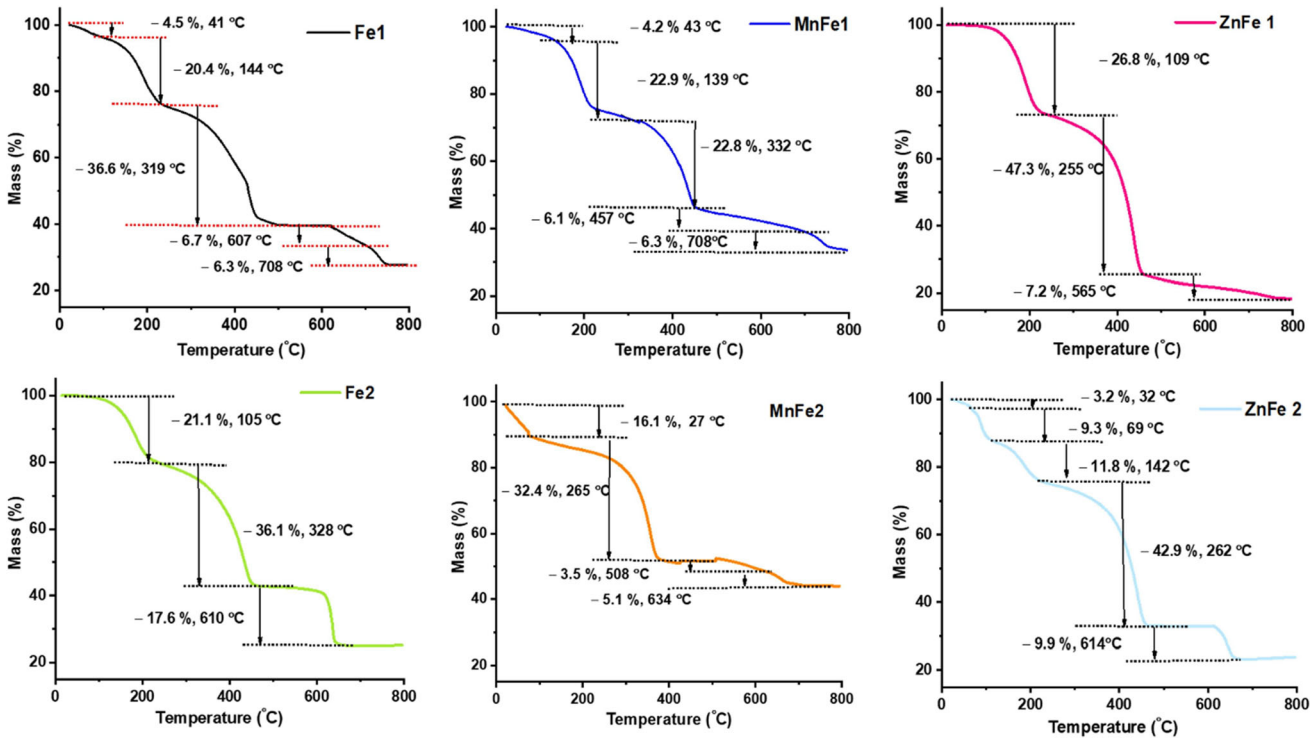

Figure 5 TGA curves of $M_xFe_{3-x}O_4$ (M = Fe, Mn, Zn) nanoferrites.

Table 3 Theoretical and experimental (AAS) molar ratios and chemical formula of $M_xFe_{3-x}O_4$ (M = Mn, Zn) nanoferrites

Nanoferrite	Molar ratio		Chemical formula	
	Theoretical	Experimental	Theoretical	Experimental
MnFe1	0.2:0.8 Mn/Fe	0.054/0.225 Mn/Fe	$Mn_{0.6}Fe_{2.4}O_4$	$Mn_{0.58}Fe_{2.42}O_4$
MnFe2	0.2:0.8 Mn/Fe	0.107/0.6 Mn/Fe	$Mn_{0.6}Fe_{2.4}O_4$	$Mn_{0.45}Fe_{2.55}$ O_4
ZnFe1	0.4:0.6 Zn/Fe	0.06/0.135 Zn/Fe	$Zn_{1.2}Fe_{1.8}O_4$	$Zn_{0.93}Fe_{2.07}O_4$
ZnFe2	0.4:0.6 Zn/Fe	0.104/0.174 Zn/Fe	$Zn_{1.2}Fe_{1.8}O_4$	$Zn_{1.12}$ $Fe_{1.87}O_4$

which is in accordance with earlier reports for Fe_3O_4.[80] Furthermore, the presence of both the + 2 and + 3 oxidation states of Fe and the formation of Fe_3O_4 rather than γ-Fe_2O_3 are thought to cause the broadness of the Fe 2*p* peaks [81].

In the case of Mn-doped Fe_3O_4 (MnFe1 and MnFe2), the presence of Mn $2p_{3/2}$ and Mn $2p_{1/2}$ spin–orbit peaks at B.E values of ~ 641.5 and 653.5 eV (MnFe1) and 641.7 and 653.8 eV (MnFe2) indicates the oxidation state of Mn^{2+} (Figures S9–S10) [3, 82, 83].

For the Zn-doped Fe_3O_4 nanoferrites, the presence of Fe in the + 3 oxidation state is indicated by two major peaks, located at 711.8 and 724.8 eV for ZnFe1 and at 711 and 724.2 eV for ZnFe2, consistent with Fe $2p_{3/2}$ and Fe $2p_{1/2}$, respectively. Furthermore, two peaks in the Zn 2*p* core-level XPS spectrum indicate Zn in the + 2 oxidation state, with B.E values of 1021.6 and 1044.8 eV (ZnFe1) and 1022.2 and 1045.4 eV (ZnFe2) and attributed to Zn $2p_{3/2}$ and Zn $2p_{1/2}$ (Figures S11–S12). The obtained values are in accordance with values reported in the literature for Zn in the + 2 oxidation state, which confirms the formation of zinc ferrite $ZnFe_2O_4$ [84, 85].

Magnetometry

Magnetisation (emu/g) as a function of the applied magnetic field (Oe) (M–H loops) was recorded using VSM at room temperature (~ 300 K) for all nanoferrites to obtain M_s, remnant magnetisation (M_r), coercivity (H_c) and normalised remanence (M_r/M_s) values (Fig. 7 and Table 3). Individual VSM plots and sample masses of nanoferrites are provided in

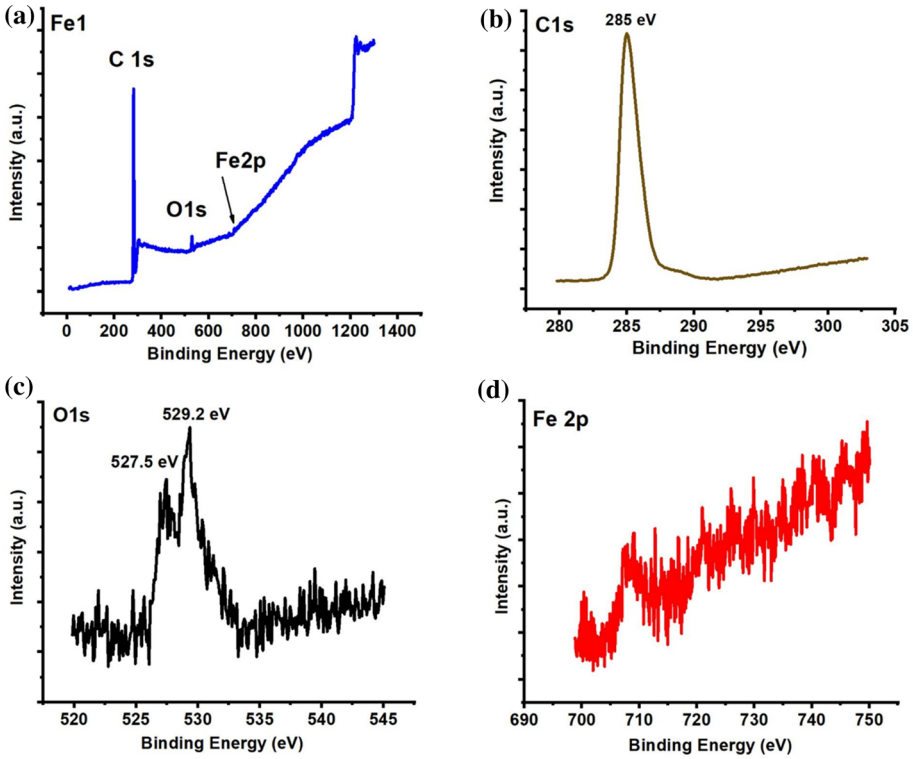

Figure 6 XPS spectra of the Fe1 nanoferrite: **a** survey scan, **b** *C1s*, **c** *O1s* and **d** Fe*2p* regional scans.

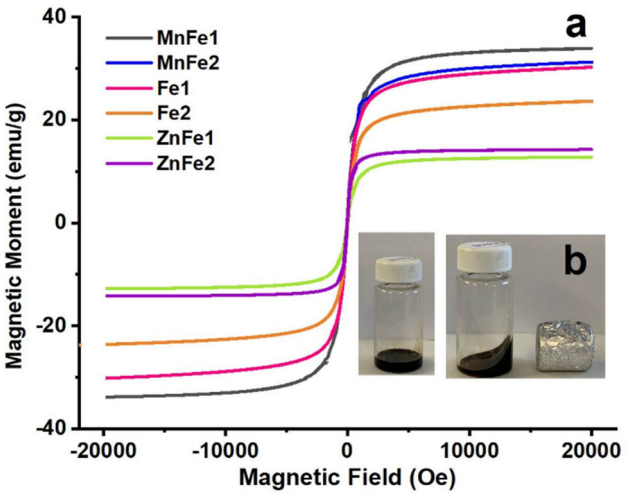

Figure 7 (a) Magnetic hysteresis loops of $M_xFe_{3-x}O_4$ (M = Fe, Mn, Zn) nanoferrites at room temperature and (b) the magnetic response of $MnFe_2$ to an external magnetic field.

Figure S13. The H_c and M_r values at low fields were almost negligible for all nanoferrites, indicating their superparamagnetic characteristics. This reveals that the superparamagnetic behaviour of Fe_3O_4 (Fe1 and Fe2) does not change after doping Zn^{2+} and Mn^{2+} ions into its spinel structure [86].

The relationship between particle size and the magnetic properties of Fe_3O_4 NPs has been examined. If the particle sizes measured with XRD and TEM are between 10 and 80 nm, particles are in single-domain state; however, particles with diameters > 80 nm present multi-domain structure. Additionally, if the measured size is < 30 nm, particles present superparamagnetic behaviour [87]. The sizes of our particles measured with TEM and XRD are < 30 nm, which indicates they are single-domain superparamagnetic feature as evidenced by VSM measurements.

Magnetisation values decreased with increased OAm content, so that M_s (Fe1) > M_s (Fe2) and M_s (MnFe1) > M_s (MnFe2). Since M_s is described on a per gram basis (emu/g), a non-magnetic coating OAm layer will diminish its value which equates a decrease in the magnetisability [88]. However, in the case of ZnFe nanoferrites, the M_s value of ZnFe2 > ZnFe1. The magnetisation difference between these particles is very small and so is most likely related to the size effect [89].

The concentration and occupation sites of doped ions are also important factors. In the crystal structure of Fe_3O_4, all Fe^{2+} ions (magnetic moment = 4 μB) occupy B sites, while the Fe^{3+} ions (magnetic moment = 5 μB) are distributed equally between A and B sites. Therefore, the net magnetisation of Fe_3O_4

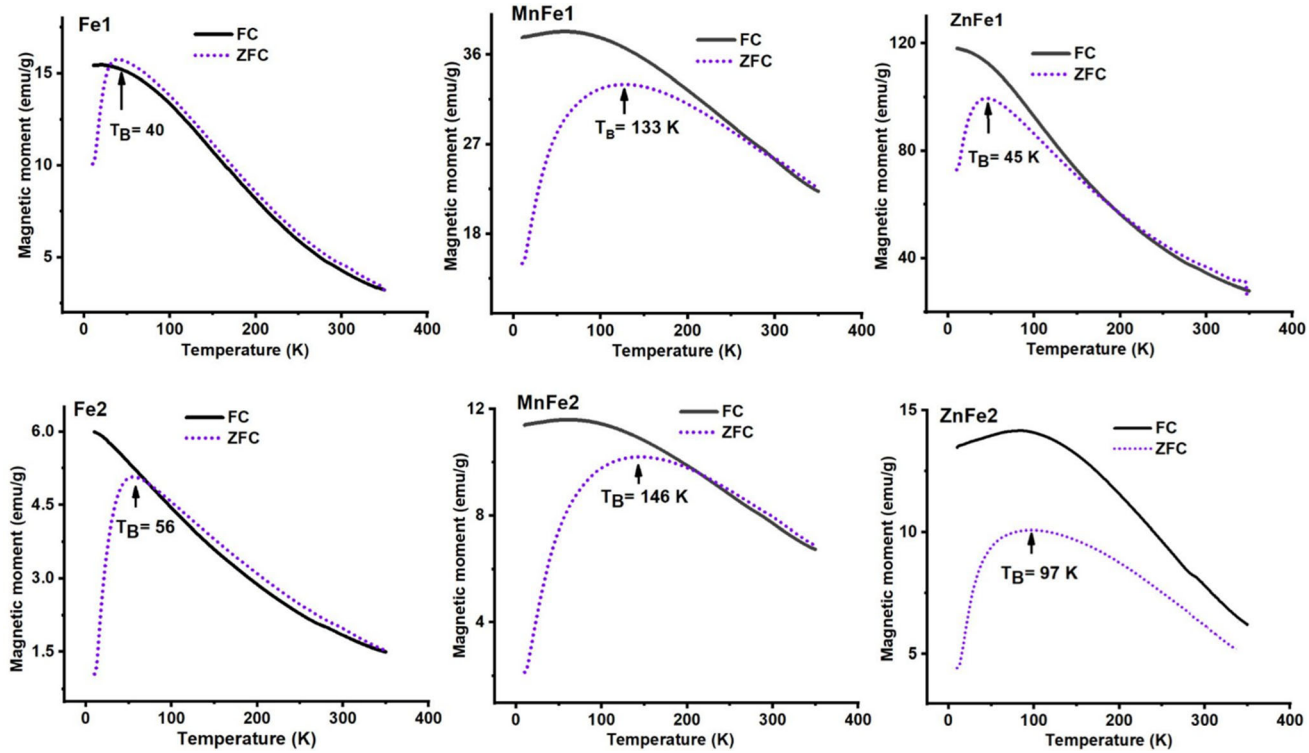

Figure 8 FC/ZFC curves of the $M_xFe_{3-x}O_4$ (M = Fe, Mn, Zn) nanoferrites recorded at a constant magnetic field of 10 Oe.

is decided by Fe^{2+} ions at B sites, as Fe^{3+} ions at A and B sites align opposite to each other and their magnetic moments cancel. When doped with Mn^{2+} or Zn^{2+} ions, the A and B sites of Fe_3O_4 can be occupied by these ions and the ferromagnetic and/or antiferromagnetic coupling interactions between Fe^{2+} and Fe^{3+} ions are modulated by their concentrations and distribution of the doped ions at the A and B sites.

For Mn-doped Fe_3O_4, the substitution of Fe^{3+} ions (5 μB) by Mn^{2+} ions (5 μB) does not change the net magnetisation of the Fe_3O_4 unit. However, if the Mn^{2+} ions (5 μB) substitute the octahedral Fe^{2+} ions (4 μB), the saturation magnetisation is expected to increase. Doping Mn^{2+} ions (0.2 mmol) into Fe_3O_4 increased the M_s from 30.2 to 33.9 emu/g for MnFe1 and from 24.8 to 31.2 emu/g for MnFe2, suggesting that Mn^{2+} substituted Fe^{2+} ions. Additionally, MnFe1 and MnFe2 nanoferrites exhibit larger sizes compared to Fe1 and Fe2, resulting in a smaller spin canting effect and higher magnetisation [67].

Doping Zn^{2+} ions (0.4 mmol) results in a reduced M_s of 14.2 emu/g for ZnFe1 and 12.7 emu/g for ZnFe2. For Zn-doped Fe_3O_4, the decrease in magnetisation is ascribed to the substitution of diamagnetic Zn^{2+} ions (0 μB) in the tetrahedral site with the Fe^{3+} ions occupying the octahedral sites, decreasing the strength of antiferromagnetic coupling interactions (the A–B superexchange interaction) of Fe^{3+} atoms and subsequent reduced magnetisability [36, 90].

Magnetisation of nanoferrites as a function of the temperature (T) (M–T curves) was investigated in the field-cooled (FC) and zero-field-cooled (ZFC) regimes under a constant magnetic field of 10 Oe to extract magnetic crystalline anisotropy energy (K_{eff}) and blocking temperature (T_B) values (Fig. 8 and Table 4). The magnetic anisotropy constant (K) was calculated for all nanoferrites using the equation, $K = 25k_BT_B/V$, where T_B is the blocking temperature, k_B is the Boltzmann's constant (1.3807×10^{-23} J K^{-1}) and V is the volume of a single nanocrystal (m^3) [2].

A marked increase in T_B was observed for Zn- and Mn-doped Fe_3O_4 NPs. This shift towards higher temperatures could be attributed to increased magneto-crystalline anisotropy of the system (Table 4). The strong coupling strength between orbital angular momentum and electron spin (L–S) can also

Table 4 Parameters of ZFC/FC and M–H hysteresis loops for $M_xFe_{3-x}O_4$ (M = Fe, Mg, Zn) nanoferrites

Nanoferrite	*Ms* (emu/g)	M_r (emu/g)	H_c (O_e)	M_r/M_s	T_B	$K \times 10^5$ (J/m^3)
Fe1	30.2	4.8	111	0.15	40	3.2
MnFe1	33.9	3.6	1.7	0.10	133	3.3
ZnFe1	14.2	2.2	60.6	0.15	45	19.9
Fe2	24.8	2.3	90.2	0.02	56	4
MnFe2	31.2	5.8	4.8	0.18	146	20.9
ZnFe2	12.7	1.18	52.4	0.09	97	12.3

contribute to higher blocking temperatures [91, 92]. The Mn-doped nanoferrites presented with broader ZFC curves. This is ascribed to the larger size distribution of NPs and increased interparticle interactions as shown by TEM results [93].

Conclusion

The synthesis of a series of low-dispersity $M_xFe_{3-x}O_4$ (M = Fe, Mn, Zn) spinel nanoferrites was achieved through the solvothermal route. The substitution of Fe^{2+} ions with paramagnetic Mn^{2+} ions resulted in improved magnetisation compared to the previous study which incorporated Mg^{2+} ions [41]. Zn^{2+} doping was effective for the formation of well-shaped nanoferrites of improved crystallinity; however, this substitution decreased the magnetisation. XPS provided evidence for the formation of $M_xFe_{3-x}O_4$ (M = Fe, Mn, Zn) spinel nanoferrites, but revealed a high organic content on the surface of the NPs. Considering the AAS results, all doped nanoferrites exhibited compositional deficiency. Our rationale to directly synthesise water-dispersible nanoferrites without subsequent treatments proved to be unsuccessful utilising PVP; however, in the future we aim to study the ratio between PVP, OAm and TOPO through which the possibility of synthesis of direct in situ water-dispersible low-dispersity particles might be achieved.

Author contributions

Research was conducted by HE under the guidance of PP. Initial paper was drafted by HE, and editing, suggestions and final checks were organised and conducted by PP.

Funding

The authors gratefully acknowledge the New Zealand International Doctoral Research Scholarships (NZIDRS) committee for their financial support.

Availability of data and material

The datasets analysed during the current study are available from the corresponding author on request.

Declarations

Conflict of interest The authors declare that they have no conflicts of interest.

Supplementary Information: The online version contains supplementary material available at https://doi.org/10.1007/s10853-021-06450-8.

References

[1] Jung-tak J, Hyunsoo N, Jae-Hyun L, Ho MS, Gyu KM, Jinwoo C (2009) Critical enhancements of MRI contrast and hyperthermic effects by dopant-controlled magnetic nanoparticles. Angew Chem Int Ed 48:1234. https://doi.org/10.1002/anie.200805149

[2] Park J, An K, Hwang Y et al (2004) Ultra-large-scale syntheses of monodisperse nanocrystals. Nat Mater 3:891. https://doi.org/10.1038/nmat1251

[3] Yang L, Ma L, Xin J et al (2017) Composition tunable manganese ferrite nanoparticles for optimized T2 contrast ability. Chem Mater 29:3038. https://doi.org/10.1021/acs.chemmater.7b00035

[4] Lasheras X, Insausti M, Gil I, de Muro et al (2016) Chemical synthesis and magnetic properties of monodisperse nickel ferrite nanoparticles for biomedical applications. J Phys Chem C 120:3492. https://doi.org/10.1021/acs.jpcc.5b10216

[5] Jung-tak J, Jooyoung L, Jiyun S et al (2018) Giant magnetic heat induction of magnesium-doped γ-Fe_2O_3

superparamagnetic nanoparticles for completely killing tumors. Adv Mater 30:1704362. https://doi.org/10.1002/adma.201704362

[6] Lee J-H, Huh Y-M, Jun Y-W et al (2006) Artificially engineered magnetic nanoparticles for ultra-sensitive molecular imaging. Nat Med 13:95. https://doi.org/10.1038/nm1467. https://www.nature.com/articles/nm1467#supplementary-information

[7] Magnetic Fluid Hyperthermia Based on Magnetic Nanoparticles: Physical Characteristics, Historical Perspective, Clinical Trials, Technological Challenges, and Recent Advances H Etemadi, PG Plieger (2020) Advanced Therapeutics 3: 2000061. Doi:https://doi.org/10.1002/adtp.202000061

[8] Li F, Liu J, Evans DG, Duan X (2004) Stoichiometric synthesis of pure MFe_2O_4 (M = Mg Co, and Ni) spinel ferrites from tailored layered double hydroxide (hydrotalcite-like) precursors. Chem Mater 16:1597. https://doi.org/10.1021/cm035248c

[9] Lee Y, Lee J, Bae CJ et al (2005) Large-scale synthesis of uniform and crystalline magnetite nanoparticles using reverse micelles as nanoreactors under reflux conditions. Adv Funct Mater 15:2036. https://doi.org/10.1002/adfm.200590040

[10] Wagle DV, Rondinone AJ, Woodward JD, Baker GA (2017) Polyol synthesis of magnetite nanocrystals in a thermostable ionic liquid. Cryst Growth Des 17:1558. https://doi.org/10.1021/acs.cgd.6b01511

[11] Deepak FL, Bañobre-López M, Carbó-Argibay E et al (2015) a systematic study of the structural and magnetic properties of Mn-, Co-, and Ni-doped colloidal magnetite nanoparticles. J Phys Chem C 119:11947. https://doi.org/10.1021/acs.jpcc.5b01575

[12] Pereira C, Pereira AM, Fernandes C et al (2012) Superparamagnetic MFe_2O_4 (M = Fe Co, Mn) nanoparticles: tuning the particle size and magnetic properties through a novel one-step coprecipitation route. Chem Mater 24:1496. https://doi.org/10.1021/cm300301c

[13] Hyeon T, Lee SS, Park J, Chung Y, Na HB (2001) Synthesis of highly crystalline and monodisperse maghemite nanocrystallites without a size-selection process. J Am Chem Soc 123:12798. https://doi.org/10.1021/ja016812s

[14] Sun S, Zeng H (2002) Size-controlled synthesis of magnetite nanoparticles. J Am Chem Soc 124:8204. https://doi.org/10.1021/ja026501x

[15] Yoo K, Jeon B-G, Chun SH et al (2016) Quantitative measurements of size-dependent magnetoelectric coupling in Fe_3O_4 nanoparticles. Nano Lett 16:7408. https://doi.org/10.1021/acs.nanolett.6b02978

[16] Tong S, Quinto CA, Zhang L, Mohindra P, Bao G (2017) Size-dependent heating of magnetic iron oxide nanoparticles. ACS Nano 11:6808. https://doi.org/10.1021/acsnano.7b01762

[17] M Dalal, J-M Greneche, B Satpati, et al. (2017). Microwave Absorption and the Magnetic Hyperthermia Applications of $Li_{0.3}Zn_{0.3}Co_{0.1}Fe_{2.3}O_4$ Nanoparticles in Multiwalled Carbon Nanotube Matrix. ACS Appl. Mater. Interfaces. 9: 40831. https://doi.org/10.1021/acsami.7b12091

[18] Mameli V, Musinu A, Ardu A et al (2016) Studying the effect of Zn-substitution on the magnetic and hyperthermic properties of cobalt ferrite nanoparticles. Nanoscale 8:10124. https://doi.org/10.1039/C6NR01303A

[19] Jeun M, Park S, Jang GH, Lee KH (2014) Tailoring $Mg_xMn_{1-x}Fe_2O_4$ superparamagnetic nanoferrites for magnetic fluid hyperthermia applications. ACS Appl Mater Interfaces 6:16487. https://doi.org/10.1021/am5057163

[20] M Jeun, JW Jeoung, S Moon, et al. (2011). Engineered superparamagnetic $Mn_{0.5}Zn_{0.5}Fe_2O_4$ nanoparticles as a heat shock protein induction agent for ocular neuroprotection in glaucoma. Biomaterials. 32: 387. https://doi.org/10.1016/j.biomaterials.2010.09.016.

[21] Khot VM, Salunkhe AB, Thorat ND, Ningthoujam RS, Pawar SH (2013) Induction heating studies of dextran coated $MgFe_2O_4$ nanoparticles for magnetic hyperthermia. Dalton Trans 42:1249. https://doi.org/10.1039/C2DT31114C

[22] He S, Zhang H, Liu Y et al (2018) Maximizing specific loss power for magnetic hyperthermia by hard-soft mixed ferrites. Small 14:1800135. https://doi.org/10.1002/smll.201800135

[23] Qu Y, Li J, Ren J, Leng J, Lin C, Shi D (2014) Enhanced magnetic fluid hyperthermia by micellar magnetic nanoclusters composed of $Mn_xZn_{1-x}Fe_2O_4$ nanoparticles for induced tumor cell apoptosis. ACS Appl Mater Interfaces 6:16867. https://doi.org/10.1021/am5042934

[24] Sathya A, Guardia P, Brescia R et al (2016) $Co_xFe_{3-x}O_4$ nanocubes for theranostic applications: effect of cobalt content and particle size. Chem Mater 28:1769. https://doi.org/10.1021/acs.chemmater.5b04780

[25] Huang J, Bu L, Xie J et al (2010) Effects of nanoparticle size on cellular uptake and liver mri with polyvinylpyrrolidone-coated iron oxide nanoparticles. ACS Nano 4:7151. https://doi.org/10.1021/nn101643u

[26] Yin PT, Shah BP, Lee KB (2014) Combined magnetic nanoparticle-based microRNA and hyperthermia therapy to enhance apoptosis in brain cancer cells. Small 10:4106. https://doi.org/10.1002/smll.201400963

[27] Panda D, Bahadur D (2007) Mechanism of cell death induced by magnetic hyperthermia with nanoparticles of γ-$Mn_xFe_{2-x}O_3$ synthesized by a single step process NK Prasad. K Rathinasamy J Mater Chem 17:5042. https://doi.org/10.1039/B708156A

[28] Munjal S, Khare N, Sivakumar B, Nair Sakthikumar D (2019) Citric acid coated $CoFe_2O_4$ nanoparticles transformed through rapid mechanochemical ligand exchange for efficient magnetic hyperthermia applications. J Magn Magn Mater 477:388. https://doi.org/10.1016/j.jmmm.2018.09.007

[29] Hu X, Ji Y, Wang M et al (2013) Water-soluble and biocompatible MnO@PVP nanoparticles for MR imaging in vitro and in vivo. J Biomed Nanotechnol 9:976. https://doi.org/10.1166/jbn.2013.1602

[30] Darr JA, Zhang J, Makwana NM, Weng X (2017) Continuous hydrothermal synthesis of inorganic nanoparticles: applications and future directions. Chem Rev 117:11125. https://doi.org/10.1021/acs.chemrev.6b00417

[31] Shi W, Song S, Zhang H (2013) Hydrothermal synthetic strategies of inorganic semiconducting nanostructures. Chem Soc Rev 42:5714. https://doi.org/10.1039/C3CS60012B

[32] Dolcet P, Diodati S, Zorzi F et al (2018) Very fast crystallisation of MFe_2O_4 spinel ferrites (M = Co, Mn, Ni, Zn) under low temperature hydrothermal conditions: a time-resolved structural investigation. Green Chem 20:2257. https://doi.org/10.1039/C8GC00086G

[33] Soto-Arreola A, Huerta-Flores AM, Mora-Hernández JM, Torres-Martínez LM (2018) Comparative study of the photocatalytic activity for hydrogen evolution of MFe_2O_4 (M = Cu, Ni) prepared by three different methods. J Photochem Photobiol A 357:20. https://doi.org/10.1016/j.jphotochem.2018.02.016

[34] Chattopadhyay A, Samanta S, Srivastava R, Mondal R, Dhar P (2019) Elemental substitution tuned magneto-elastoviscous behavior of nanoscale ferrite MFe_2O_4 (M = Mn, Fe Co, Ni) based complex fluids. J Magn Magn Mater 491:165622. https://doi.org/10.1016/j.jmmm.2019.165622

[35] Bastianello M, Gross S, Elm MT (2019) Thermal stability, electrochemical and structural characterization of hydrothermally synthesised cobalt ferrite ($CoFe_2O_4$). RSC Adv 9:33282. https://doi.org/10.1039/C9RA06310B

[36] Tsay C-Y, Chiu Y-C, Tseng Y-K (2019) Investigation on structural, magnetic, and FMR properties for hydrothermally-synthesized magnesium-zinc ferrite nanoparticles. Phys B 570:29. https://doi.org/10.1016/j.physb.2019.05.037

[37] Sun F, Zeng Q, Tian W, Zhu Y, Jiang W (2019) Magnetic MFe_2O_4-Ag_2O (M = Zn Co, & Ni) composite photocatalysts and their application for dye wastewater treatment. J Environ Chem Eng 7:103011. https://doi.org/10.1016/j.jece.2019.103011

[38] Georgiadou V, Kokotidou C, Le Droumaguet B, Carbonnier B, Choli-Papadopoulou T, Dendrinou-Samara C (2014) Oleylamine as a beneficial agent for the synthesis of $CoFe_2O_4$ nanoparticles with potential biomedical uses. Dalton Trans 43:6377. https://doi.org/10.1039/C3DT53179A

[39] Vamvakidis K, Katsikini M, Sakellari D, Paloura EC, Kalogirou O, Dendrinou-Samara C (2014) Reducing the inversion degree of $MnFe_2O_4$ nanoparticles through synthesis to enhance magnetization: evaluation of their 1H NMR relaxation and heating efficiency. Dalton Trans 43:12754. https://doi.org/10.1039/C4DT00162A

[40] Menelaou M, Georgoula K, Simeonidis K, Dendrinou-Samara C (2014) Evaluation of nickel ferrite nanoparticles coated with oleylamine by NMR relaxation measurements and magnetic hyperthermia. Dalton Trans 43:3626. https://doi.org/10.1039/C3DT52860J

[41] Etemadi H, Plieger PG (2020) Improvements in the organic-phase hydrothermal synthesis of monodisperse $M_xFe_{3-x}O_4$ (M = Fe, Mg, Zn) spinel nanoferrites for magnetic fluid hyperthermia application. ACS Omega 5:18091. https://doi.org/10.1021/acsomega.0c01641

[42] Lu X, Niu M, Qiao R, Gao M (2008) Superdispersible PVP-coated Fe_3O_4 nanocrystals prepared by a "one-pot" reaction. J Phys Chem B 112:14390. https://doi.org/10.1021/jp8025072

[43] Halda Ribeiro A, Ersöz B, Tremel W, Jakob G, Asadi K (2017) Effect of precursor concentration on size evolution of iron oxide nanoparticles H Sharifi Dehsari. CrystEngComm 19:6694. https://doi.org/10.1039/C7CE01406F

[44] Mahdavinia GR, Etemadi H, Soleymani F (2015) Magnetic/pH-responsive beads based on caboxymethyl chitosan and κ-carrageenan and controlled drug release. Carbohydr Polym 128:112. https://doi.org/10.1016/j.carbpol.2015.04.022

[45] Mahdavinia GR, Etemadi H (2014) In situ synthesis of magnetic CaraPVA IPN nanocomposite hydrogels and controlled drug release. Mater Sci Eng, C 45:250. https://doi.org/10.1016/j.msec.2014.09.023

[46] Ruiz A, -Baltazar, R Esparza, G Rosas, R perez, (2015) Effect of the surfactant on the growth and oxidation of iron nanoparticles. J Nanomater 2015:8. https://doi.org/10.1155/2015/240948

[47] Kim W, Suh C-Y, Cho S-W et al (2012) A new method for the identification and quantification of magnetite–maghemite mixture using conventional X-ray diffraction technique. Talanta 94:348. https://doi.org/10.1016/j.talanta.2012.03.001

[48] Huang Y, Ding D, Zhu M et al (2015) Facile synthesis of α-Fe_2O_3 nanodisk with superior photocatalytic performance and mechanism insight. Sci Technol Adv Mater 16:014801. https://doi.org/10.1088/1468-6996/16/1/014801

[49] Yin Y, Zeng M, Liu J et al (2016) Enhanced high-frequency absorption of anisotropic Fe_3O_4/graphene nanocomposites. Sci Rep 6:25075. https://doi.org/10.1038/srep25075

[50] YV Kolen'ko, M Bañobre-López, C Rodríguez-Abreu et al (2014) Large-scale synthesis of colloidal Fe_3O_4 nanoparticles exhibiting high heating efficiency in magnetic hyperthermia. J Phys Chem C 118:8691. https://doi.org/10.1021/jp500816u

[51] Kollu P, Kumar PR, Santosh C, Kim DK, Grace AN (2015) A high capacity $MnFe_2O_4$/rGO nanocomposite for Li and Na-ion battery applications. RSC Adv 5:63304. https://doi.org/10.1039/C5RA11439J

[52] Feng L, Xuan Z, Zhao H et al (2014) MnO_2 prepared by hydrothermal method and electrochemical performance as anode for lithium-ion battery. Nanoscale Res Lett 9:290. https://doi.org/10.1186/1556-276X-9-290

[53] Zhu J, Tang S, Xie H, Dai Y, Meng X (2014) Hierarchically porous mno$_2$ microspheres doped with homogeneously distributed Fe_3O_4 nanoparticles for supercapacitors. ACS Appl Mater Interfaces 6:17637. https://doi.org/10.1021/am505622c

[54] Saha P, Rakshit R, Mandal K (2019) Enhanced magnetic properties of Zn doped Fe_3O_4 nano hollow spheres for better bio-medical applications. J Magn Magn Mater 475:130. https://doi.org/10.1016/j.jmmm.2018.11.061

[55] Kulkarni SD, Kumbar S, Menon SG, Choudhari KS, S C, (2016) Magnetically separable core–shell $ZnFe_2O_4$@ZnO nanoparticles for visible light photodegradation of methyl orange. Mater Res Bull 77:70. https://doi.org/10.1016/j.materresbull.2016.01.022

[56] Sun T, Hao H, Hao W-t, Yi S-m, Li X-p, Li J-r (2014) Preparation and antibacterial properties of titanium-doped ZnO from different zinc salts. Nanoscale Res Lett 9:98. https://doi.org/10.1186/1556-276X-9-98

[57] Perrière J, Hebert C, Nistor M, Millon E, Ganem JJ, Jedrecy N (2015) $Zn_{1-x}Fe_xO$ films: from transparent Fe-diluted ZnO wurtzite to magnetic Zn-diluted Fe_3O_4 spinel. J Mater Chem C 3:11239. https://doi.org/10.1039/C5TC02090E

[58] Hwang SO, Kim CH, Myung Y et al (2008) Synthesis of vertically aligned manganese-doped Fe_3O_4 nanowire arrays and their excellent room-temperature gas sensing ability. J Phys Chem C 112:13911. https://doi.org/10.1021/jp802943z

[59] Liu J, Bin Y, Matsuo M (2012) Magnetic behavior of zn-doped Fe_3O_4 nanoparticles estimated in terms of crystal domain size. J Phys Chem C 116:134. https://doi.org/10.1021/jp207354s

[60] Li X, Liu E, Zhang Z, Xu Z, Xu F (2019) Solvothermal synthesis, characterization and magnetic properties of nearly superparamagnetic Zn-doped Fe_3O_4 nanoparticles. J Mater Sci: Mater Electron 30:3177. https://doi.org/10.1007/s10854-018-00640-y

[61] Ahmed MA, Rady KE-S, El-Shokrofy KM, Arais AA, Shams MS (2014) The influence of Zn^{2+} ions substitution on the microstructure and transport properties of Mn-Zn nanoferrites. MSA 05(13):11. https://doi.org/10.4236/msa.2014.513095

[62] Cai J, Miao YQ, Yu BZ, Ma P, Li L, Fan HM (2017) Large-scale, facile transfer of oleic acid-stabilized iron oxide nanoparticles to the aqueous phase for biological applications. Langmuir 33:1662. https://doi.org/10.1021/acs.langmuir.6b03360

[63] Willis AL, Turro NJ, O'Brien S (2005) Spectroscopic characterization of the surface of iron oxide nanocrystals. Chem Mater 17:5970. https://doi.org/10.1021/cm051370v

[64] Bastami TR, Entezari MH, Hu QH, Hartono SB, Qiao SZ (2012) Role of polymeric surfactants on the growth of manganese ferrite nanoparticles. Chem Eng J 210:157. https://doi.org/10.1016/j.cej.2012.08.031

[65] Roca AG, Morales MP, O'Grady K, Serna CJ (2006) Structural and magnetic properties of uniform magnetite nanoparticles prepared by high temperature decomposition of organic precursors. Nanotechnology 17:2783. https://doi.org/10.1088/0957-4484/17/11/010

[66] Ayyappan S, Mahadevan S, Chandramohan P, Srinivasan MP, Philip J, Raj B (2010) Influence of Co^{2+} ion concentration on the size, magnetic properties, and purity of $CoFe_2O_4$ spinel ferrite nanoparticles. J Phys Chem C 114:6334. https://doi.org/10.1021/jp911966p

[67] Del Bianco L, Spizzo F, Barucca G et al (2019) Mechanism of magnetic heating in Mn-doped magnetite nanoparticles and the role of intertwined structural and magnetic properties. Nanoscale 11:10896. https://doi.org/10.1039/C9NR03131F

[68] Li L, Ruotolo A, Leung CW, Jiang CP, Pong PWT (2015) Characterization and bio-binding ability study on size-controllable highly monodisperse magnetic nanoparticles. Microelectron Eng 144:61. https://doi.org/10.1016/j.mee.2015.03.057

[69] Yu BY, Kwak S-Y (2011) Self-assembled mesoporous Co and Ni-ferrite spherical clusters consisting of spinel nanocrystals prepared using a template-free approach. Dalton Trans 40:9989. https://doi.org/10.1039/C1DT10650C

[70] Dubal DP, Kim WB, Lokhande CD (2012) Galvanostatically deposited Fe: MnO_2 electrodes for supercapacitor application. J Phys Chem Solids 73:18. https://doi.org/10.1016/j.jpcs.2011.09.005

[71] Hu L, de Montferrand C, Lalatonne Y, Motte L, Brioude A (2012) Effect of cobalt doping concentration on the crystalline structure and magnetic properties of monodisperse $Co_xFe_{3-x}O_4$ nanoparticles within nonpolar and aqueous solvents. J Phys Chem C 116:4349. https://doi.org/10.1021/jp205088x

[72] Oberdick SD, Abdelgawad A, Moya C et al (2018) Spin canting across core/shell $Fe_3O_4/Mn_xFe_{3-x}O_4$ nanoparticles. Sci Rep 8:3425. https://doi.org/10.1038/s41598-018-21626-0

[73] Otero-Lorenzo R, Fantechi E, Sangregorio C, Salgueiriño V (2016) Solvothermally driven Mn doping and clustering of iron oxide nanoparticles for heat delivery applications. Chem Eur J 22:6666. https://doi.org/10.1002/chem.201505049

[74] Song Q, Ding Y, Wang ZL, Zhang ZJ (2007) Tuning the thermal stability of molecular precursors for the nonhydrolytic synthesis of magnetic $MnFe_2O_4$ spinel nanocrystals. Chem Mater 19:4633. https://doi.org/10.1021/cm070990o

[75] Wang W, Tang B, Ju B, Gao Z, Xiu J, Zhang S (2017) Fe_3O_4-functionalized graphene nanosheet embedded phase change material composites: efficient magnetic- and sunlight-driven energy conversion and storage. J Mater Chem A 5:958. https://doi.org/10.1039/C6TA07144A

[76] Ansari SM, Sinha BB, Phase D et al (2019) Particle size, morphology, and chemical composition controlled $CoFe_2O_4$ nanoparticles with tunable magnetic properties via oleic acid based solvothermal synthesis for application in electronic devices. ACS Appl Nano Mater 2:1828. https://doi.org/10.1021/acsanm.8b02009

[77] Iacovita C, Stiufiuc R, Radu T et al (2015) Polyethylene glycol-mediated synthesis of cubic iron oxide nanoparticles with high heating power. Nanoscale Res Lett 10:391. https://doi.org/10.1186/s11671-015-1091-0

[78] Li M, Xiong Y, Liu X et al (2015) Facile synthesis of electrospun MFe_2O_4 (M = Co, Ni, Cu, Mn) spinel nanofibers with excellent electrocatalytic properties for oxygen evolution and hydrogen peroxide reduction. Nanoscale 7:8920. https://doi.org/10.1039/C4NR07243J

[79] Sathishkumar G, Logeshwaran V, Sarathbabu S et al (2018) Green synthesis of magnetic Fe_3O_4 nanoparticles using Couroupita guianensis Aubl. fruit extract for their antibacterial and cytotoxicity activities. Artif Cells Nanomed Biotechnol 46:589. https://doi.org/10.1080/21691401.2017.1332635

[80] Zhang M, Zhao F, Yang Y et al (2020) Synthesis, characterization and catalytic behavior of MFe_2O_4 (M = Ni, Zn and Co) nanoparticles on the thermal decomposition of TKX-50. J Therm Anal Calorim 141:1413. https://doi.org/10.1007/s10973-019-09102-x

[81] Han F, Ma L, Sun Q, Lei C, Lu A (2014) Rationally designed carbon-coated Fe_3O_4 coaxial nanotubes with hierarchical porosity as high-rate anodes for lithium ion batteries. Nano Res 7:1706. https://doi.org/10.1007/s12274-014-0531-y

[82] Liu Y, Zhang N, Yu C, Jiao L, Chen J (2016) $MnFe_2O_4$@C nanofibers as high-performance anode for sodium-ion batteries. Nano Lett 16:3321. https://doi.org/10.1021/acs.nanolett.6b00942

[83] Long X-Y, Li J-Y, Sheng D, Lian H-Z (2017) Spinel-type manganese ferrite ($MnFe_2O_4$) microspheres: A novel affinity probe for selective and fast enrichment of phosphopeptides. Talanta 166:36. https://doi.org/10.1016/j.talanta.2017.01.025

[84] Guo X, Zhu H, Si M et al (2014) $ZnFe_2O_4$ nanotubes: microstructure and magnetic properties. J Phys Chem C 118:30145. https://doi.org/10.1021/jp507991e

[85] Baird N, Losovyj Y, Yuzik-Klimova EY et al (2016) Zinc-containing magnetic oxides stabilized by a polymer: one phase or two? ACS Appl Mater Interfaces 8:891. https://doi.org/10.1021/acsami.5b10302

[86] Neuberger T, Schöpf B, Hofmann H, Hofmann M, von Rechenberg B (2005) Superparamagnetic nanoparticles for biomedical applications: possibilities and limitations of a new drug delivery system. J Magn Magn Mater 293:483. https://doi.org/10.1016/j.jmmm.2005.01.064

[87] Li Q, Kartikowati CW, Horie S, Ogi T, Iwaki T, Okuyama K (2017) Correlation between particle size/domain structure and magnetic properties of highly crystalline Fe3O4 nanoparticles. Sci Rep 7:9894. https://doi.org/10.1038/s41598-017-09897-5

[88] Kolhatkar AG, Jamison AC, Litvinov D, Willson RC, Lee TR (2013) Tuning the magnetic properties of nanoparticles. Int J Mol Sci 14:15977

[89] Darbandi M, Stromberg F, Landers J et al (2012) Nanoscale size effect on surface spin canting in iron oxide nanoparticles synthesized by the microemulsion method. J Phys D: Appl Phys 45:195001. https://doi.org/10.1088/0022-3727/45/19/195001

[90] Ibrahim I, Ali IO, Salama TM, Bahgat AA, Mohamed MM (2016) Synthesis of magnetically recyclable spinel ferrite (MFe_2O_4, M=Zn Co, Mn) nanocrystals engineered by sol gel-hydrothermal technology: High catalytic performances for nitroarenes reduction. Appl Catal B 181:389. https://doi.org/10.1016/j.apcatb.2015.08.005

[91] Nandwana V, Ryoo S-R, Kanthala S et al (2016) Engineered theranostic magnetic nanostructures: role of composition and surface coating on magnetic resonance imaging contrast and thermal activation. ACS Appl Mater Interfaces 8:6953. https://doi.org/10.1021/acsami.6b01377

[92] Song Q, Zhang ZJ (2006) Correlation between spin−orbital coupling and the superparamagnetic properties in magnetite and cobalt ferrite spinel nanocrystals. J Phys Chem B 110:11205. https://doi.org/10.1021/jp060577o

[93] Casula MF, Conca E, Bakaimi I et al (2016) Manganese doped-iron oxide nanoparticle clusters and their potential as agents for magnetic resonance imaging and hyperthermia. PCCP 18:16848. https://doi.org/10.1039/C6CP02094A